

## Electronic Supplementary Information

### One-pot Synthesis of Defect Engineered Carbon Nitride for Highly Efficient Visible Light Photocatalysis

Xuying Li,<sup>a</sup> Haoxin Mai,<sup>\*a</sup> Xingdong Wang,<sup>b</sup> Zongli Xie,<sup>b</sup> Junlin Lu,<sup>a</sup> Xiaoming Wen,<sup>a</sup> Salvy P. Russo,<sup>c</sup> Dehong Chen<sup>\*a</sup> and Rachel A. Caruso<sup>\*a</sup>

a Applied Chemistry and Environmental Science, School of Science, STEM College, RMIT University, Melbourne, Vic. 3000, Australia.

b CSIRO Manufacturing, Private bag 10, Clayton South, Vic. 3169, Australia

c ARC Centre of Excellence in Exciton Science, School of Science, RMIT University, Melbourne, Victoria 3000, Australia

\*Corresponding authors: haoxin.mai@rmit.edu.au; dehong.chen@rmit.edu.au; rachel.caruso@rmit.edu.au

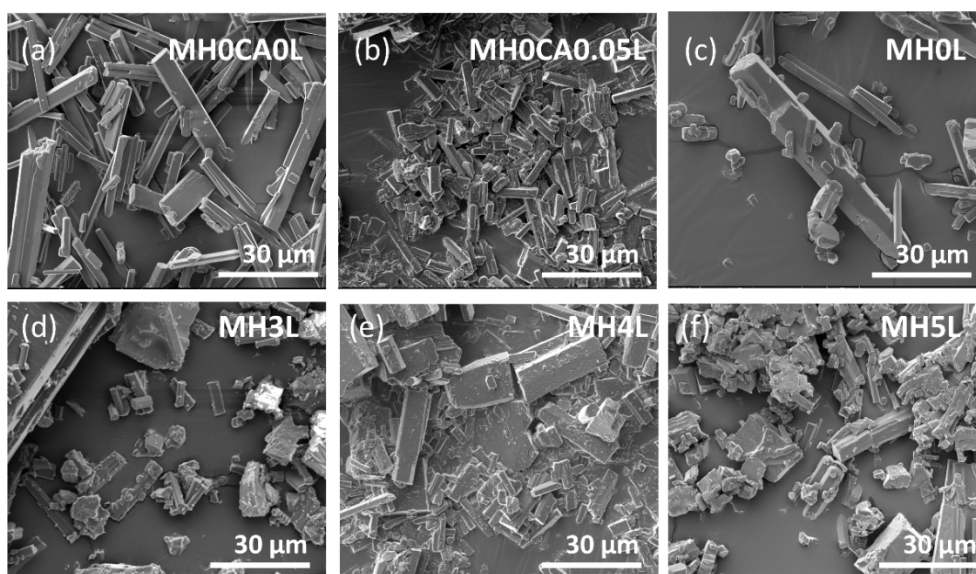


**Fig. S1.** SEM images of the MH precursors prepared (a) without CA or LiOH: MH0CA0L, (b) without CA and with 0.05 mL LiOH: MH0CA0.05L, and (c-f) with 0.5 g CA and different volumes of 5 M LiOH: (c) MH0L, (d) MH3L, (e) MH4L and (f) MH5L.

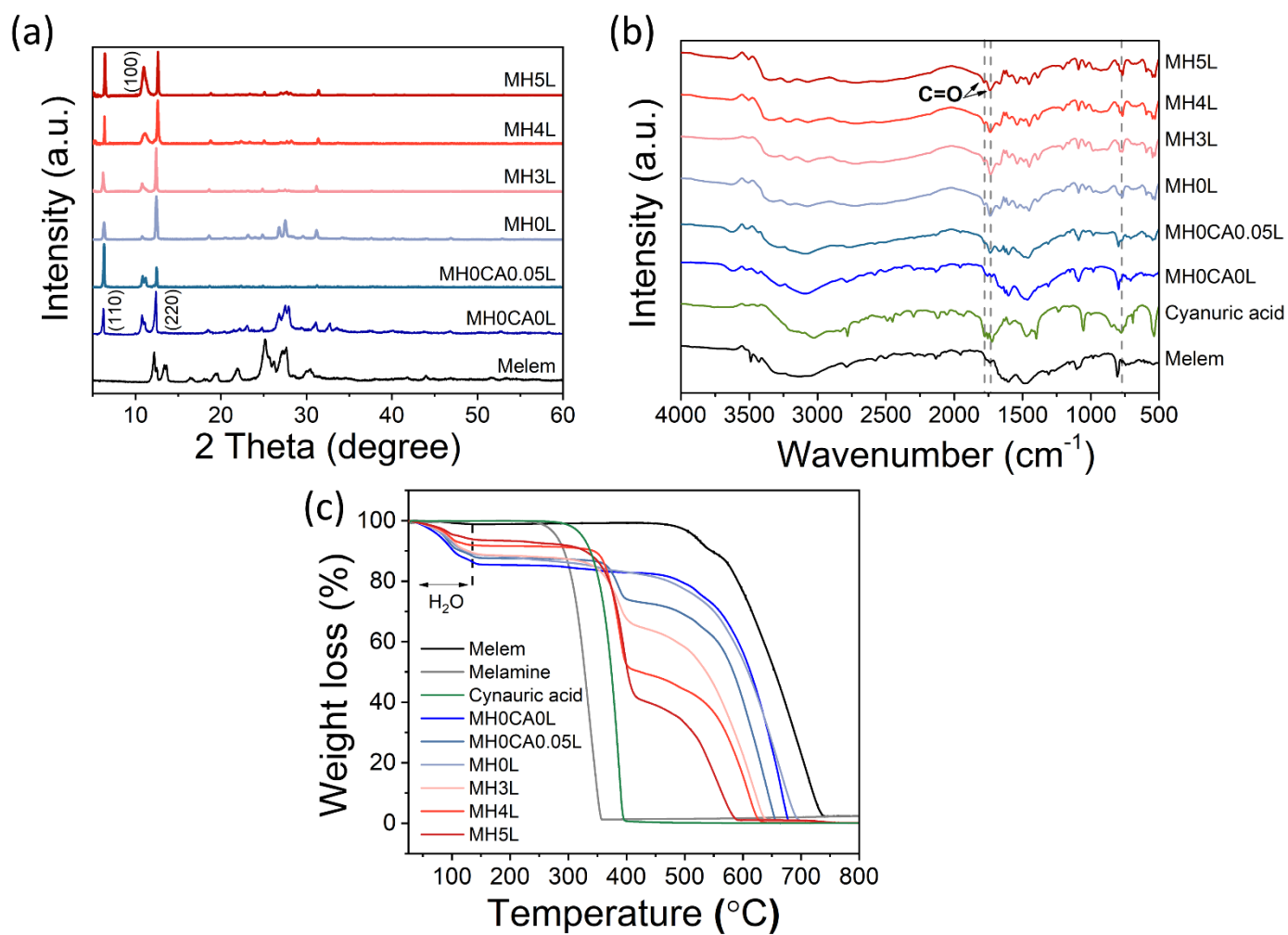


**Fig. S2.** (a) XRD patterns of MH0CA0L, MH0CA0.05L, MH0L, MH3L, MH4L and MH5L. (b) FTIR spectra and (c) TGA curves of melem, melamine, cyanuric acid, MH0CA0L, MH0CA0.05L, MH0L, MH3L, MH4L and MH5L.

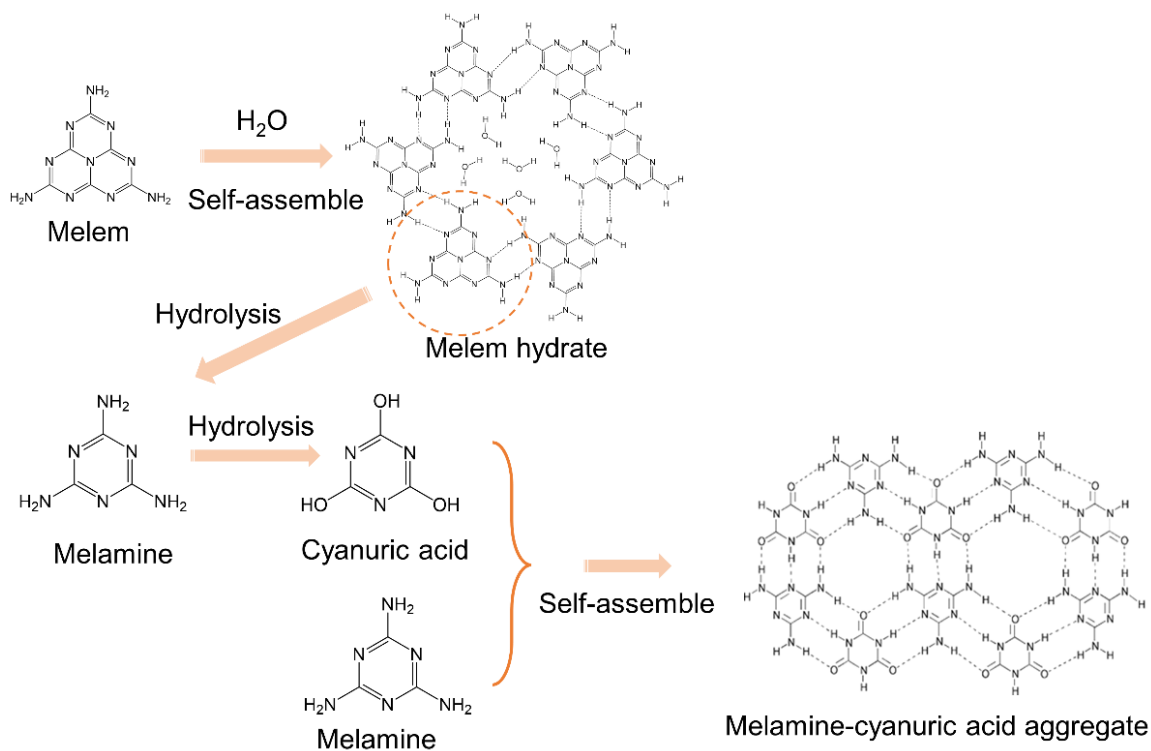


**Fig. S3.** Plausible formation process of melem hydrate (MH) and melamine-cyanuric acid (MCA) aggregate.

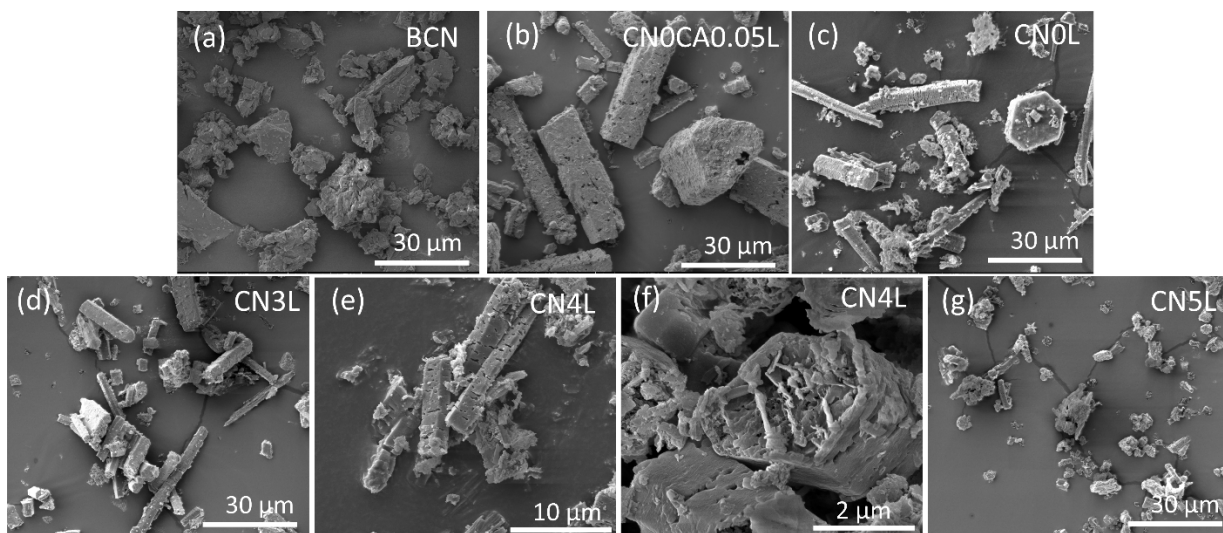


**Fig. S4.** SEM images of (a) BCN, (b) CN prepared without CA and with 0.5 mL LiOH: CN0CA0.05L, and (c-g) CN samples prepared with different volumes of 5 M LiOH: (c) CN0L, (d) CN3L, (e) and (f) CN4L and (g) CN5L.

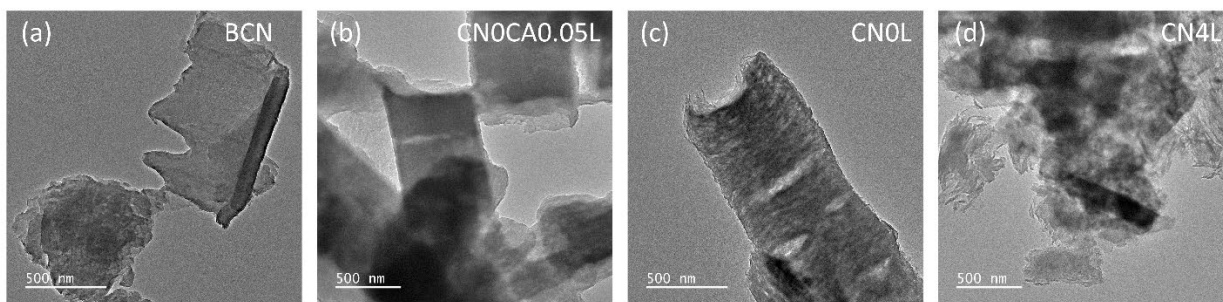


**Fig. S5.** TEM images of (a) BCN, (b) CN0CA0.05L, (c) CN0L and (d) CN4L.

**Table S1.** BET surface areas of the BCN and CN samples.

Sample	Surface area ( $\text{m}^2 \cdot \text{g}^{-1}$ ) <sup>a</sup>	Pore volume ( $\text{cm}^3 \cdot \text{g}^{-1}$ ) <sup>b</sup>	Pore size (nm) <sup>c</sup>
BCN	12.3	0.06	15.8
CN0CA0.05L	7.9	0.06	14.5
CN0L	73.1	0.26	14.9
CN3L	29.6	0.15	19.6
CN4L	31.1	0.16	20.6
CN5L	35.9	0.17	21.0

The CN samples were denoted as CN0CA0.05L (sample prepared without CA and with 0.05 mL 5 M LiOH) or CNxL, where x is the volume of 5 M LiOH (0, 3.0, 4.0 and 5.0 mL) used during synthesis, L = LiOH. a) Specific surface area obtained by BET method, b) single point adsorption total pore volume at  $P/P_0 = 0.983$  based on the BJH adsorption branch model and c) peak of the pore size distribution.

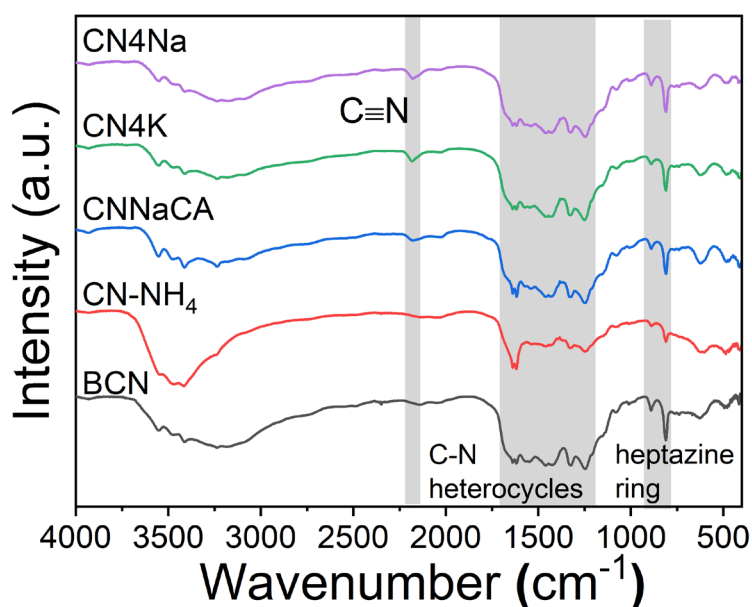


**Fig. S6.** FTIR spectra of BCN, CN-NH<sub>4</sub>, CNNaCA, CN4K and CN4Na.

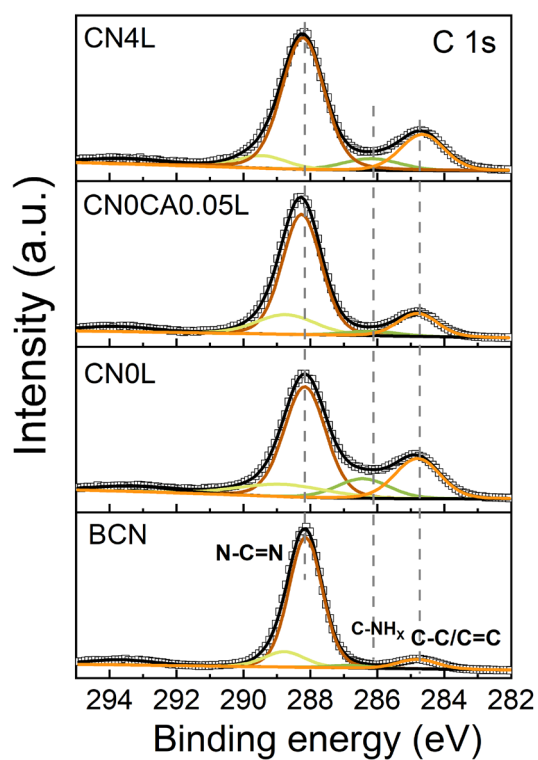


**Fig. S7.** High-resolution C 1s XPS spectra of BCN, CN0L, CN0CA0.05L and CN4L.

**Table S2.** C/N atomic ratio for BCN and CN samples obtained from XPS and EDS.

Sample	C/N atomic ratio from XPS	C/N atomic ratio from EDS
BCN	0.69	0.68
CN0CA0.05L	0.70	0.72
CN0L	0.98	0.95
CN3L	0.88	0.86
CN4L	0.84	0.84
CN5L	0.86	0.88

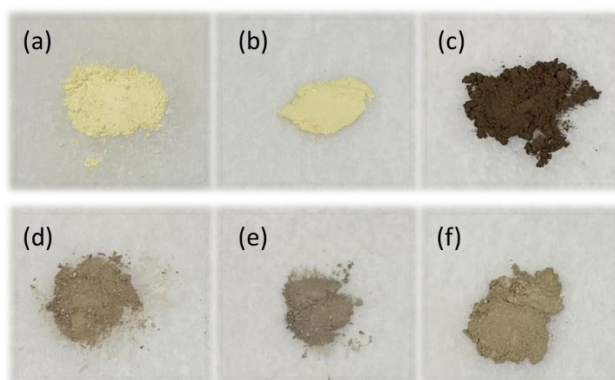


**Fig. S8.** Photographs of (a) BCN, (b) CN0CA0.05L, (c) CN0L, (d) CN3L, (e) CN4L and (f) CN5L.

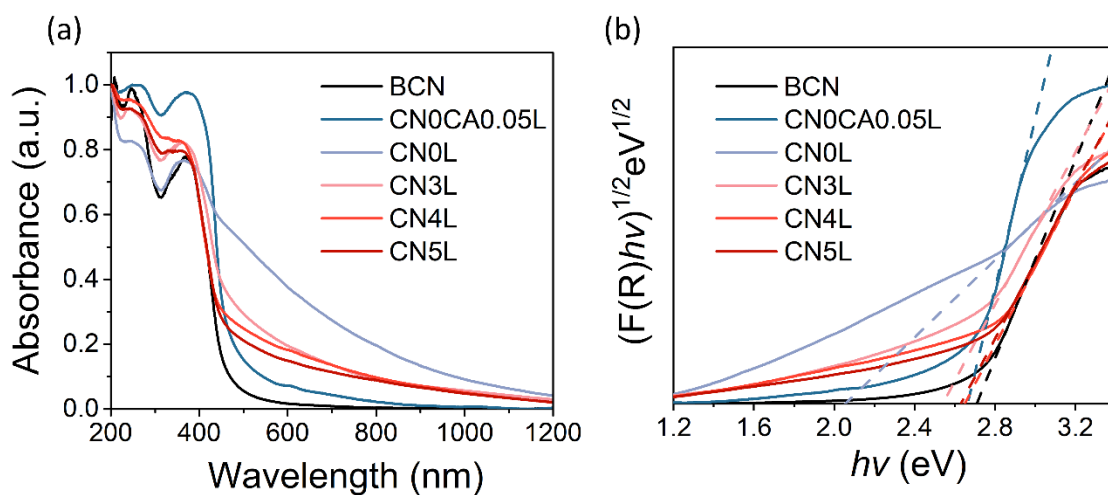


**Fig. S9.** (a) UV-vis diffuse reflectance spectra and (b) plots of the Kubelka–Munk function versus photon energy of BCN and CN samples.

**Table S3.** Band gap energy and band structure of BCN and CN samples.

Sample	Band gap energy (eV)	VB (V vs NHE)	CB (V vs NHE)
BCN	2.72	1.88	-0.84
CN0CA0.05L	2.67	2.04	-0.63
CN0L	2.35	1.97	-0.38
CN3L	2.52	2.03	-0.49
CN4L	2.65	2.08	-0.57
CN5L	2.64	2.11	-0.53

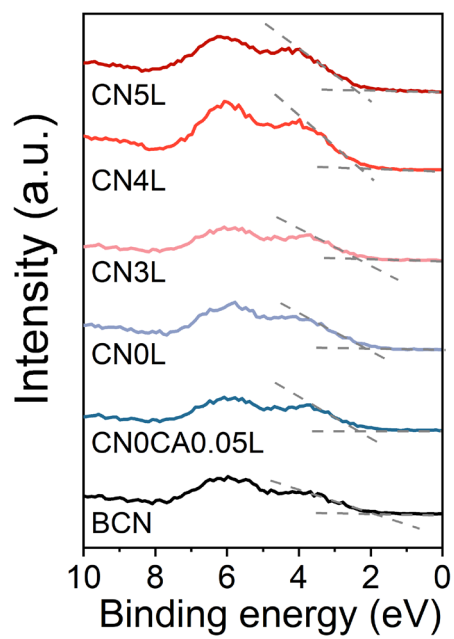


**Fig. S10.** XPS valence band determination of BCN and CN samples.

## Note 1: Density Functional Theory (DFT) Calculations

The structure of the single-layered BCN was constructed based on structure characterisation (e.g., XRD,  $^{13}\text{C}$  NMR, FTIR) and published results ( $\text{C}_{24}\text{N}_{36}\text{H}_{12}$ , **Fig. S11a**).<sup>1, 2</sup> In all the structural models, the spheres coloured white, blue and grey represent atoms of H, N and C, respectively. Based on the convergence tests, a plane-wave cut-off energy of 500 eV was selected, and the  $\Gamma$ -centred k-points mesh of  $12 \times 12 \times 1$  was employed for sampling the Brillouin zones. The atomic positions were fully relaxed until the force on each atom was smaller than  $0.01 \text{ eV}/\text{\AA}$  and the convergence threshold for the self-consistent field was  $10^{-5} \text{ eV}$ . To calculate band structure, the selected k-path was  $\Gamma (0, 0, 0) - \text{X} (0.5, 0, 0) - \text{S} (0.5, 0.5, 0) - \text{Y} (0, 0.5, 0) - \Gamma (0, 0, 0) - \text{S} (0.5, 0.5, 0)$ .<sup>3</sup>

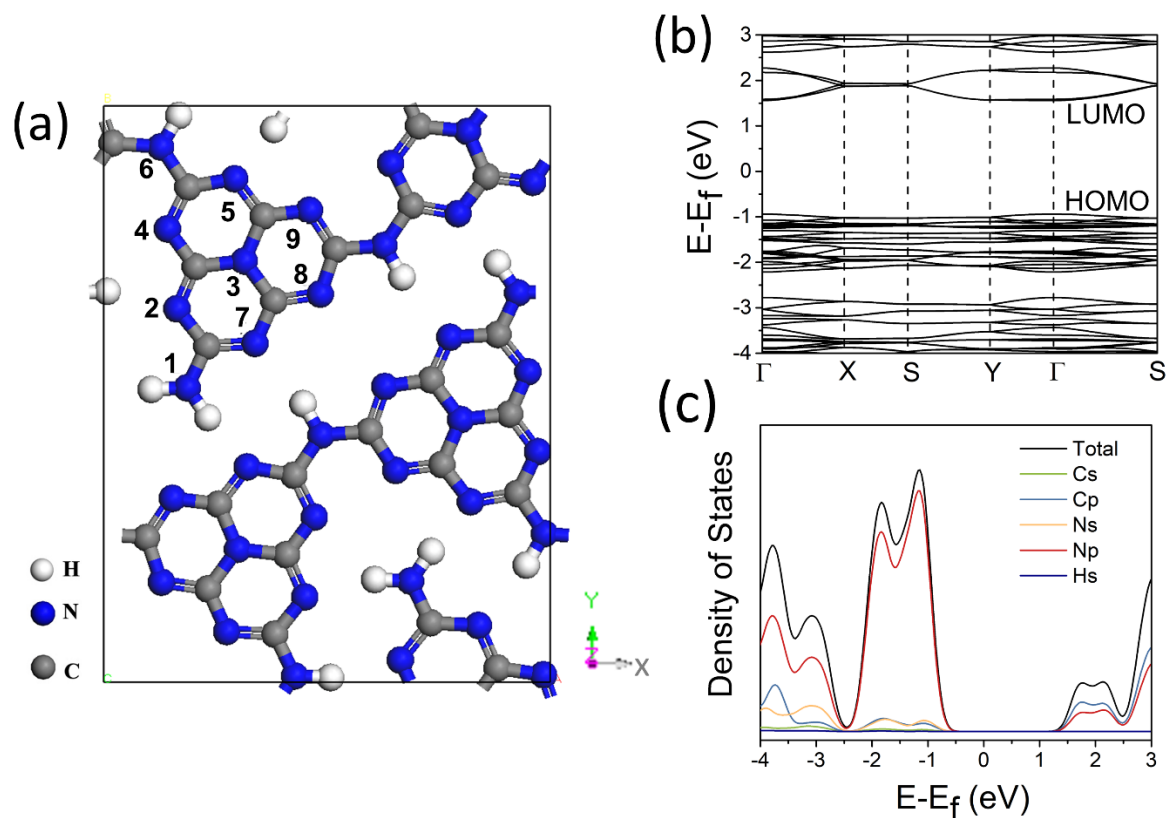


**Fig. S11.** (a) Structure model, (b) calculated band structure and (c) corresponding density of states (DOS) for single-layered BCN.

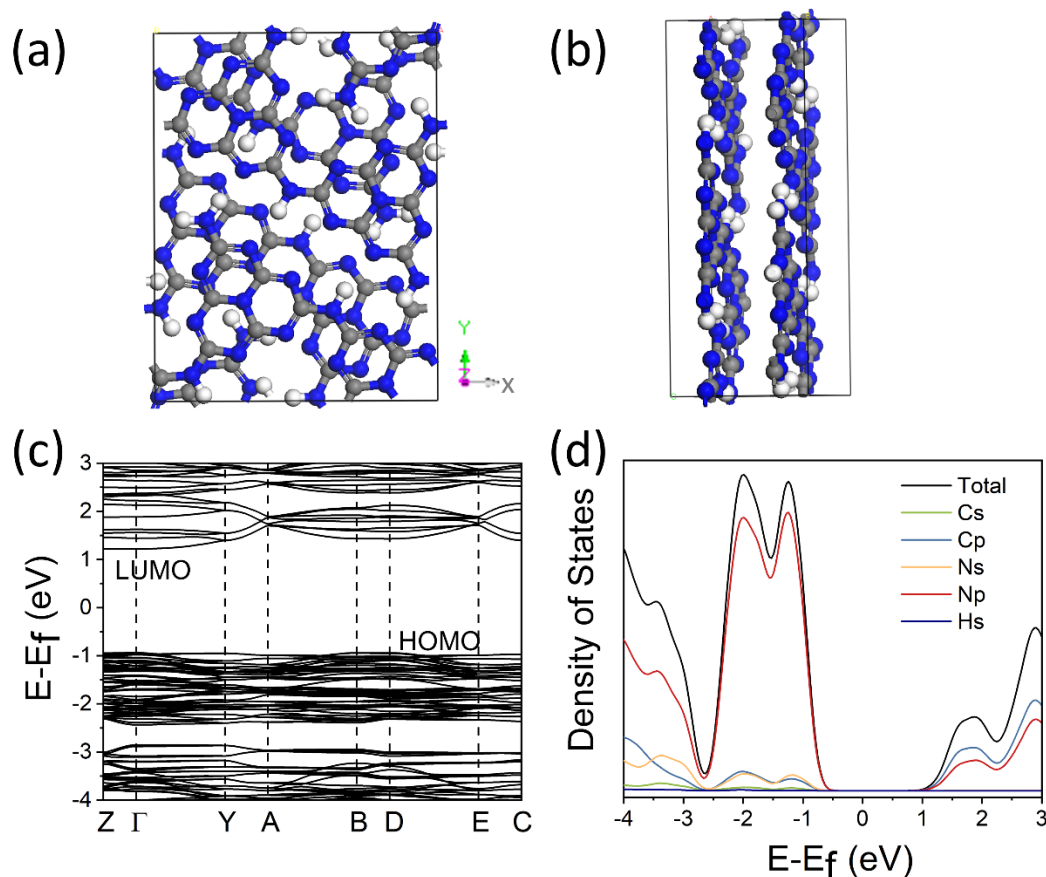


**Fig. S12.** (a) Front-view and (b) side-view structure models, (c) calculated band structure and (d) corresponding DOS for 2-layered BCN.

**Fig. S11b** shows the band structure of the BCN. The valance band maximum (VBM) and conduction band minimum (CBM) were located at the  $\Gamma$  point in the first Brillouin zone, indicating that the BCN (melon) possessed a direct bandgap.<sup>4</sup> The calculated bandgap was 2.48 eV (**Fig. S11b**), with a 9.1% difference from the experimental bandgap (2.72 eV, **Fig. S9b**).<sup>5</sup> The density of states (DOS) calculation clearly revealed that the VBM was dominated by the N 2p orbitals with a small contribution from the N 2s and C 2p orbitals, while the CBM mainly consisted of the N 2p and C 2p orbitals (**Fig. S11c**).

As the BCN could potentially adopt a 2-layered structure (**Fig. S12a, b**),<sup>6</sup> we compared the band structure and DOS between the single-layered BCN and the 2-layered BCN ( $\Gamma$ -centred k-points mesh of  $8 \times 16 \times 6$  was employed for sampling the Brillouin zones of the 2-layered BCN, and the selected k-path was Z (0, 0, 0.5) –  $\Gamma$  (0, 0, 0) – Y (0, 0.5, 0) – A (0.5, 0.5, 0) – B (0.5, 0, 0) – D (0.5, 0, 0.5) – E (0.5, 0.5, 0.5) – C (0, 0.5, 0.5)). The DOS profiles and bandgaps were similar (**Fig. S12c and d** compared with **Fig. S11b and c**). The 2-layered BCN possessed a direct bandgap of 2.16 eV with the VBM and CBM located at the  $\Gamma$  point in the first Brillouin

zone (**Fig. S12c**). The 2-layered BCN exhibited more bands in the CB and VB, because the number of atoms in the 2-layered BCN was twice that of the single-layered BCN, but no intermediate bands were observed in the forbidden gap. According to the DOS calculations, the VBM was mainly composed of N 2p orbitals, and the CBM of N 2p and C 2p orbitals, resembling those of the single-layered BCN. As the bandgap of the single-layered BCN was closer to the experimental value, and the DOS profiles of the single-layered and 2-layered BCN were very similar, single-layered CNs will be used in the following calculations.

**Table S4.** The total energy of the C-doped melon with the C dopant located at different sites. (See Fig. S11 for site locations).

Site for C dopant	Total energy (eV)
N1	-555.2
N2	-562.1
N3	-562.0
N4	-556.4
N5	-558.9
N6	-555.6
N7	-555.0
N8	-556.1
N9	-558.6

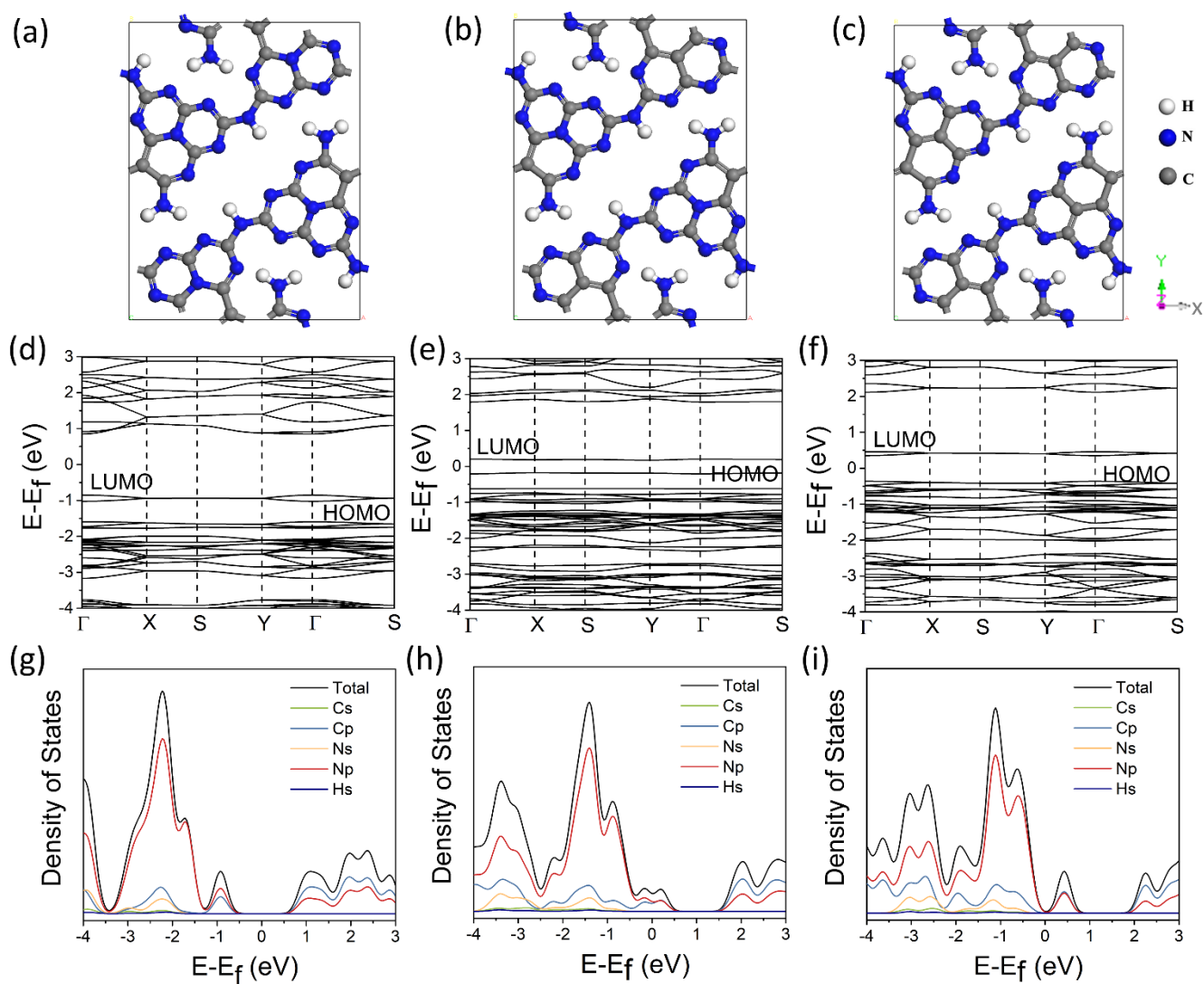


**Fig. S13.** (a, b, c) Structure models, (d, e, f) calculated band structure and (g, h, i) corresponding DOS for C<sub>28</sub>N<sub>32</sub>H<sub>12</sub>, C<sub>30</sub>N<sub>30</sub>H<sub>12</sub> and C<sub>32</sub>N<sub>28</sub>H<sub>12</sub>, respectively.

To simulate the C-doped melon structures, one of the N atoms in each heptazine ring was replaced by a C atom, forming  $C_{28}N_{32}H_{12}$  ( $C/N = 0.875$ ). As all the N atoms in the heptazine ring were not equivalent based on crystal periodic relationship, nine irreducible configurations could be generated (**Fig. S11a**). To identify the N atom that would most likely be substituted and simplify the following calculations, the total energy among these nine irreducible configurations was compared (**Table S4**). The maximum energy differences among these nine configurations were 7.1 eV, and the configuration where the C dopant was located at the N2 site possessed the lowest energy (**Fig. S13a**), indicating that this configuration was the most thermodynamically favoured. Likewise, the most stable configurations for  $C_{30}N_{30}H_{12}$  and  $C_{32}N_{28}H_{12}$  were determined by their total energy and are shown in **Fig. S13b** and **c**. Note that the C/N ratio of CN0L was  $\sim 1$ , therefore we suggest that the configuration of  $C_{30}N_{30}H_{12}$  (**Fig. S13c**) would be a typical structure for CN0L.

For the calculation of band structures of the C-doped melon, the selected k-path was  $\Gamma (0, 0, 0) - X (0.5, 0, 0) - S (0.5, 0.5, 0) - Y (0, 0.5, 0) - \Gamma (0, 0, 0) - S (0.5, 0.5, 0)$ . The band structure (**Fig. S13b**) and DOS (**Fig. S13c**) of  $C_{28}N_{32}H_{12}$  showed a slight decrease in bandgap (from 2.48 eV to 2.41 eV) and the presence of two new mid-gap band levels ( $\sim 0.6 - 0.8$  eV above the VBM), enhancing absorption in the visible light region as shown in **Fig. S9a**. Distinct by different composition of the VBM (which mainly consisted of N 2p orbitals), the mid-gap levels consisted of N 2p orbitals and C 2p orbitals, indicating that they were derived from the C dopants (**Fig. S13c**). Further increasing the C dopant amount would not induce a sharp change in bandgap ( $C_{30}N_{30}H_{12}$  2.40 eV,  $C_{32}N_{28}H_{12}$  2.44 eV). The mid-gap band levels located at  $\sim 0.4$  eV and  $\sim 0.8$  eV above the VBM in  $C_{30}N_{30}H_{12}$  (**Fig. S13e**) and at  $\sim 0.6$  eV and  $\sim 0.8$  eV above the VBM in  $C_{32}N_{28}H_{12}$  (**Fig. S13h**). The compositions of the VBM, CBM and the mid-gap levels in  $C_{30}N_{30}H_{12}$  and  $C_{32}N_{28}H_{12}$  remained the same as those of  $C_{28}N_{32}H_{12}$  (**Fig. S13f** and **i**). However, it is worth noting that distinct from  $C_{28}N_{32}H_{12}$  in which all the mid-gap levels were occupied, the upper mid-gap level in  $C_{30}N_{30}H_{12}$  and all the mid-gap levels in  $C_{32}N_{28}H_{12}$  were empty (**Fig. S13b, e** and **h**), leading to a much smaller gap between the highest occupied molecular orbitals (HOMO) and the lowest unoccupied molecular orbitals (LUMO) in these samples. Therefore, the samples with  $C/N > 0.875$  (e.g., CN0L) exhibited a strong absorption tail in the visible light region (**Fig. S9a**).

In the cases of CN3L and CN4L, where  $C/N \sim 0.85$  and the cyano groups were formed by replacing the C-NH<sub>2</sub> groups, there are two possible configurations, breaking the C-CN<sub>2</sub> bond or the N-CN<sub>2</sub> bond in  $C_{28}N_{32}H_{12}$  (**Fig. S14a, b** and **c**). The total energy of these two

configurations are -558.3 eV and -559.1 eV, respectively, indicating that the configuration formed by breaking the N-CN<sub>H</sub> bond was more stable (**Fig. S14c**). Therefore, the configuration shown in **Fig. S14c** was considered to be thermodynamically stable for the C<sub>28</sub>N<sub>32</sub>H<sub>12</sub> with a small amount of cyano groups (e.g., CN<sub>4</sub>L, labelled as C<sub>28</sub>N<sub>32</sub>H<sub>12</sub>-cyano), which was in agreement with the <sup>13</sup>C NMR and FTIR results.

The profiles of the DOS and band structure of the C<sub>28</sub>N<sub>32</sub>H<sub>12</sub>-cyano were similar with those of C<sub>28</sub>N<sub>32</sub>H<sub>12</sub>. Two mid-gap bands were positioned at ~0.6 – 0.8 eV above the VBM (**Fig. S14d**). The DOS showed that the CBM consisted of N 2p orbitals and C 2p orbitals, and the VBM mainly of N 2p orbitals, and the mid-gap levels of N 2p orbitals and C 2p orbitals (**Fig. S14e**).

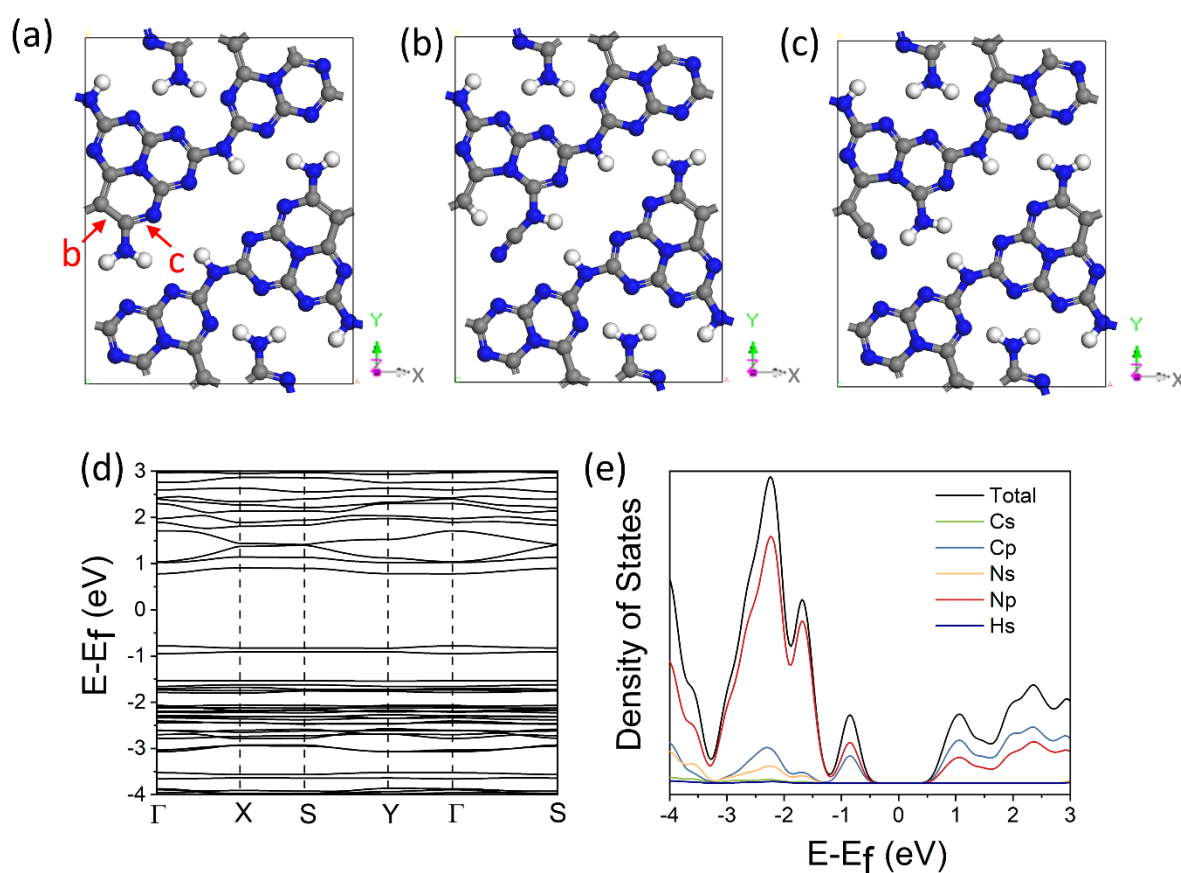


**Fig. S14.** (a) Structure model for C<sub>28</sub>N<sub>32</sub>H<sub>12</sub> with red arrows indicating two possible cyano group formation configurations, with breaking of the (b) C-CN<sub>H</sub> bond or (c) N-CN<sub>H</sub> bond. (d) Calculated band structures and (e) corresponding DOS for C<sub>28</sub>N<sub>32</sub>H<sub>12</sub>-cyano CN.

To simulate the structures in which more cyano groups were formed (e.g., CN5L), we replaced another three C-NH<sub>2</sub> groups with cyano groups based on the configuration shown in **Fig. S15** (labelled as C<sub>28</sub>N<sub>32</sub>H<sub>12</sub>-4cyano). Three mid-gap bands were identified in this configuration. The VBM and the mid-gap bands in C<sub>28</sub>N<sub>32</sub>H<sub>12</sub>-4cyano were less dispersive than those in C<sub>28</sub>N<sub>32</sub>H<sub>12</sub> and C<sub>28</sub>N<sub>32</sub>H<sub>12</sub>-cyano, indicating the electrons were highly localized. According to the DOS, the extra mid-gap band formed in this configuration mainly consisted of N 2p orbitals with a small amount of C 2p and N 2s orbitals.

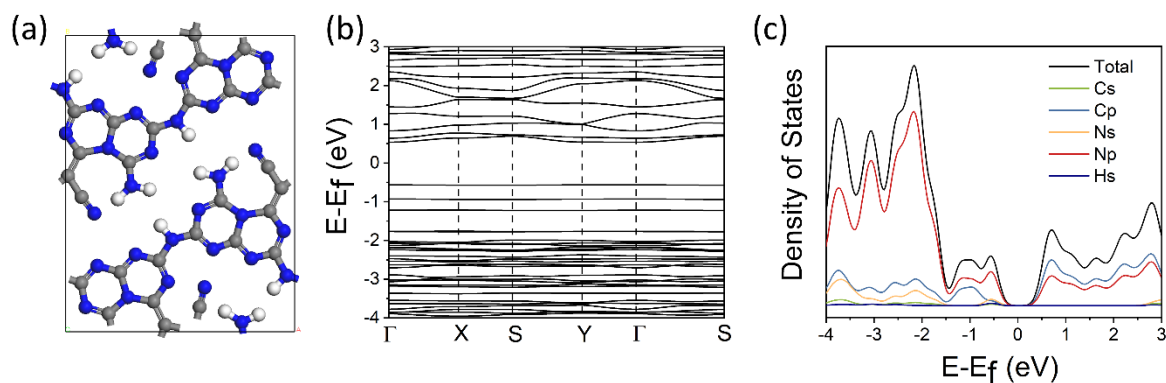


**Fig. S15.** (a) Structure model, (b) calculated band structures and (c) corresponding DOS for single-layered C-doped CN with more cyano groups (4 per unit cell).

To calculate the electron density distribution in the excited state, the geometrical optimisation of the configurations was performed by manually setting the frontier states electronic occupation for each k-point through the VASP tags FERWE and FERDO.

The effective mass of the charge carriers could be found from equation (1) based on the energy band structure:

$$E(k) = E_0 + \hbar^2 k^2 / 2m \quad (1)$$

where  $m$  is effective mass of the charge carriers,  $k$  is the wave vector,  $E_0$  is the energy of the band edge,  $\hbar$  is the reduced Plank constant and  $E(k)$  is the energy of an electron or a hole at wave vector  $k$  in that band. As a result,  $m$  could be obtained by equation (2):<sup>7</sup>

$$m = \hbar^2 \times \left( \frac{\partial^2 E}{\partial k^2} \right)^{-1} \quad (2)$$

The effective mass of an electron ( $m_e$ ) and hole ( $m_h$ ), therefore, could be determined via parabolic fitting of the bands around the CBM and VBM and calculating their  $\frac{\partial^2 E}{\partial k^2}$ , respectively.<sup>8</sup>

**Table S5.** Effective masses of the electron ( $m_e$ ) and hole ( $m_h$ ) and the calculated reduced mass ( $\mu$ ) relative to the different crystal facets.

CN samples	$m_e$	$m_h$	$\mu$
C <sub>24</sub> N <sub>36</sub> H <sub>12</sub> (BCN)	0.57 $m_0$	-1.79 $m_0$	0.43 $m_0$
C <sub>28</sub> N <sub>32</sub> H <sub>12</sub>	0.41 $m_0$	-2.17 $m_0$	0.35 $m_0$
C <sub>30</sub> N <sub>30</sub> H <sub>12</sub> (CN0L)	1.43 $m_0$	-3.85 $m_0$	1.04 $m_0$
C <sub>32</sub> N <sub>28</sub> H <sub>12</sub>	1.52 $m_0$	-4.55 $m_0$	1.14 $m_0$
C <sub>28</sub> N <sub>32</sub> H <sub>12</sub> -cyano (CN4L)	0.83 $m_0$	-2.94 $m_0$	0.66 $m_0$
C <sub>28</sub> N <sub>32</sub> H <sub>12</sub> -4cyano (CN5L)	1.14 $m_0$	-10 $m_0$	1.02 $m_0$

$\mu$  represents reduced mass,  $\mu = \left( 1/m_e + 1/|m_h| \right)^{-1}$ .  $m_0$  is the free electron mass.

**Table S6.** Fitted lifetimes and their percentages for BCN and CN samples.

Sample	$\tau_1$ (ns) [A1%]	$\tau_2$ (ns) [A2%]	$\tau_3$ (ns) [A3%]	Average lifetime ( $\tau_{ave}$ , ns)
BCN	0.46 [97.78]	1.34 [2.11]	4.43 [0.11]	0.55
CN0CA0.05L	0.35 [75.80]	1.05 [21.71]	3.69 [2.48]	1.14
CN0L	0.48 [46.12]	1.34 [41.80]	4.51 [12.08]	2.50
CN4L	0.45 [48.51]	1.32 [42.50]	4.37 [8.99]	2.18
CN5L	0.48 [53.81]	1.27 [38.37]	4.04 [7.82]	1.90

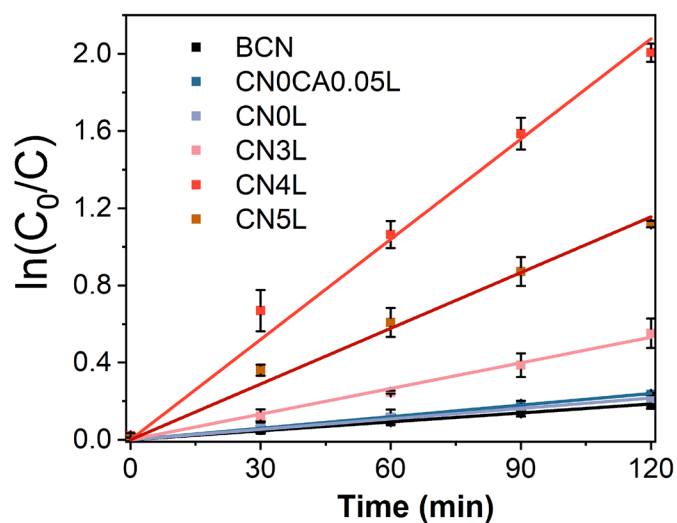


**Fig. S16.** The  $\ln(C_0/C)$  vs. time plots for the photocatalytic degradation of TC-HCl under visible light in the presence of BCN and CN samples.

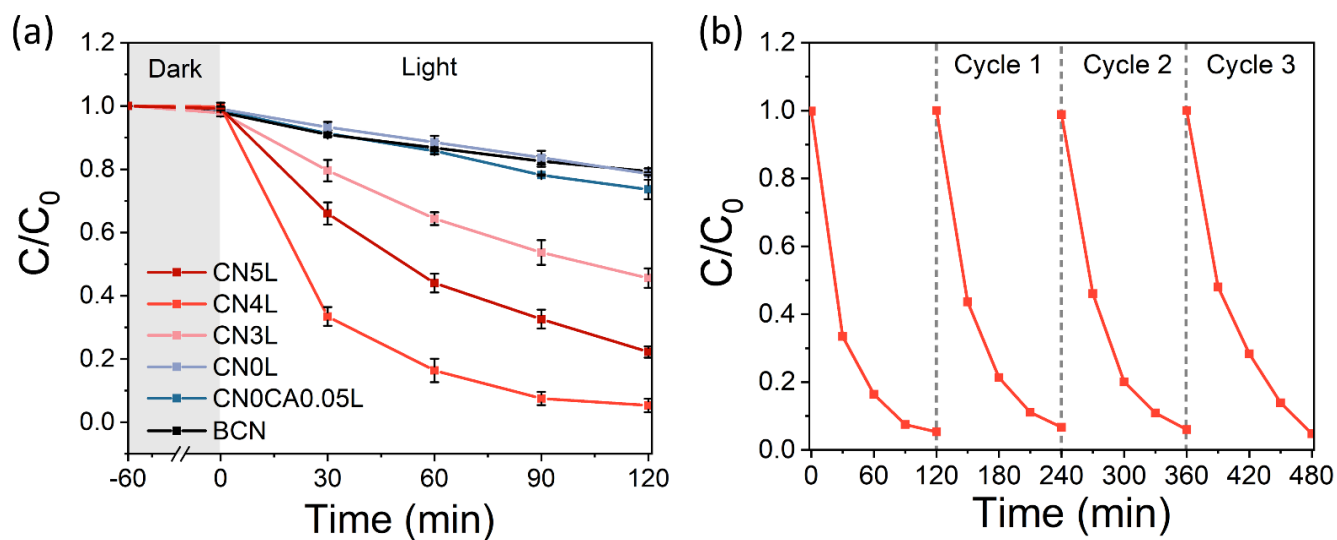


**Fig. S17.** (a) Photocatalytic degradation of RhB under visible light in the presence of BCN or CN samples. Error bars were derived from the results of three tests. (b) Recycling test of CN4L for the degradation of RhB under visible light.

**Table S7.** Organic pollutant degradation over photocatalysts reported in published work.

Photocatalyst	Light source	Pollutant type and concentration	Photocatalyst (mg)	Degradation efficiency	Ref.
Fe-doped TiO <sub>2</sub>	500 W Hg mid-pressure immersion lamp ( $\lambda > 320$ nm)	10 <sup>-5</sup> M 4-CP; 10 <sup>-5</sup> M MO	100	65% 4-CP in 240 min; 95% MO in 240 min	9
CaWO <sub>4</sub> microcrystals	UV-C light ( $\lambda = 254$ nm), ultrasonic bath (40 kHz and 70 W)	10 <sup>-5</sup> mol·L <sup>-1</sup> RhB	50	96% in 200 min	10
WO <sub>3</sub> /g-C <sub>3</sub> N <sub>4</sub>	300 W Xe lamp ( $\lambda > 400$ nm)	20 ppm dinitro butyl phenol	50	98.1% MPB in 60 min; 98.2% of APAP in 30 min	11
LaNi <sub>0.8</sub> Fe <sub>0.2</sub> O <sub>3</sub> /g-C <sub>3</sub> N <sub>4</sub>	300 W Xe lamp ( $\lambda > 400$ nm)	10 ppm TC	20	86.1% in 120 min	12
N-deficient g-C <sub>3</sub> N <sub>4</sub>	30 W LED lamp (410 < $\lambda$ < 760nm)	10 ppm TC	200	60% in 120 min	13
N-deficient g-C <sub>3</sub> N <sub>4</sub>	300 W Xe lamp ( $\lambda > 400$ nm)	10 ppm RhB; 10 ppm TC	10	95% TC in 60 min; ~100% RhB in 60 min	14
4,6-dimethyl-2-hydroxypyrimidine-doped and cyano defects co-modified g-C <sub>3</sub> N <sub>4</sub>	Xe lamp ( $\lambda > 400$ nm)	20	10	74% in 60 min	15
Cl-doped g-C <sub>3</sub> N <sub>4</sub>	300 W Xe lamp ( $\lambda > 400$ nm)	10 ppm TC	50	92% in 120 min	16
P and Mo co-doped g-C <sub>3</sub> N <sub>4</sub>	Xe lamp ( $\lambda > 420$ nm)	10 ppm TC	50	69% in 120 min	17
C-doped cyano group modified CN	500 W Xe lamp ( $\lambda > 420$ nm)	10 ppm RhB; 10 ppm TC-HCl	25	96% RhB in 120 min; 87% TC-HCl in 120 min	This work

4-CP: 4-chlorophenol; MO: Methyl orange; RhB: rhodamine B; g-C<sub>3</sub>N<sub>4</sub>: graphitic carbon nitride; TC: tetracycline; APAP: acetaminophen; MPB: methylparaben.

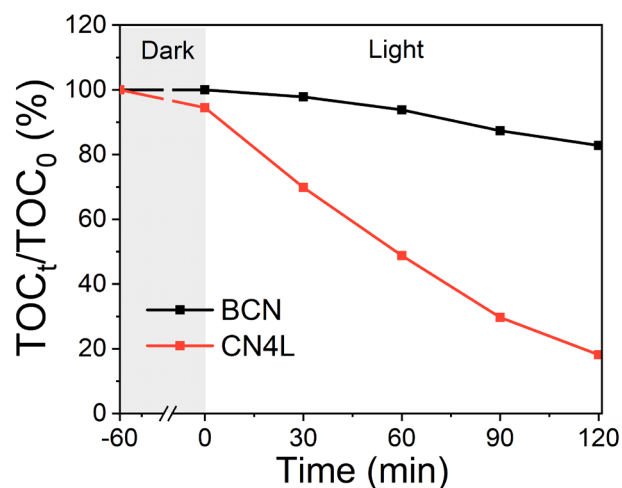


**Fig. S18.** TOC content in RhB solution under visible light in the presence of BCN and CN4L, where TOC<sub>t</sub> and TOC<sub>0</sub> are the TOC at time t and in the initial solution, respectively.

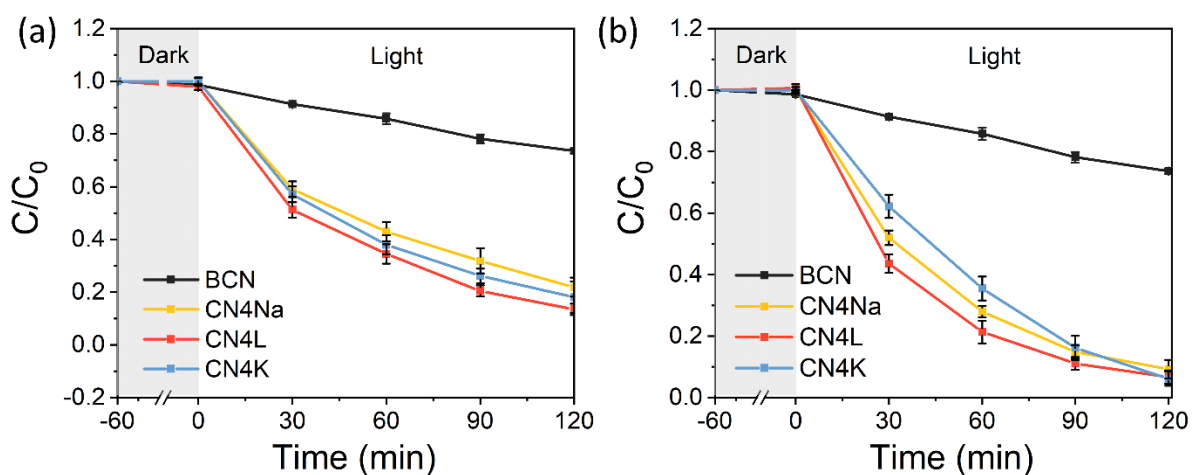


**Fig. S19.** Visible light photocatalytic degradation of (a) TC-HCl and (b) RhB over BCN and CN samples prepared with the addition of 4 mL 5 M NaOH (CN4Na), LiOH (CN4L) or KOH (CN4K).

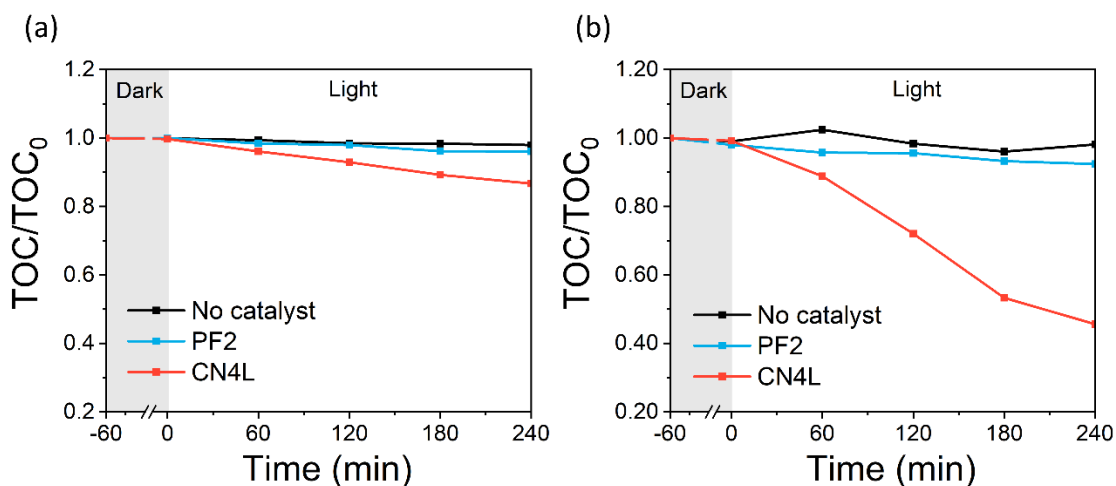


**Fig. S20.** TOC content change in (a) municipal and (b) hospital wastewater solution under visible light in the presence of PF2 and CN4L.

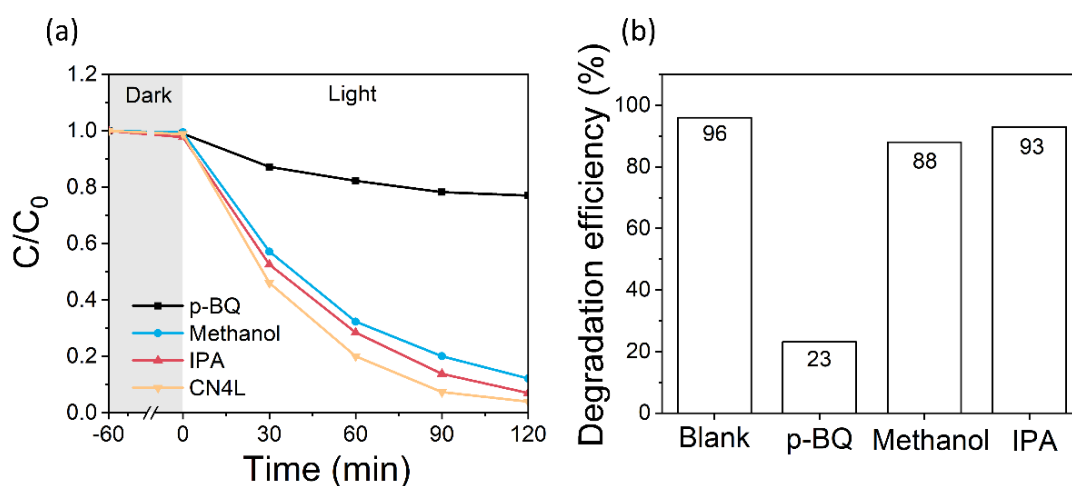


**Fig. S21.** Visible light photodegradation of RhB with and without radical scavengers over CN4L.

Control experiments with the presence of radical scavengers (IPA for hydroxyl radicals, methanol for holes, and p-BQ for superoxide radicals) were conducted to test the active radicals in the photodegradation process of RhB. As shown in **Fig. S21**, the photocatalytic activity of CN4L reduced dramatically with the addition of p-BQ, indicating the predominant role of the superoxide radicals in the degradation process. In comparison, the addition of methanol caused a slight decrease in the photocatalytic activity of CN4L, implying that a small portion of the reactive radicals were attributed to the photoexcited holes. Additionally, the photocatalytic activity dropped from 96% to 81% when adding IPA, confirming the contribution of hydroxyl radicals.

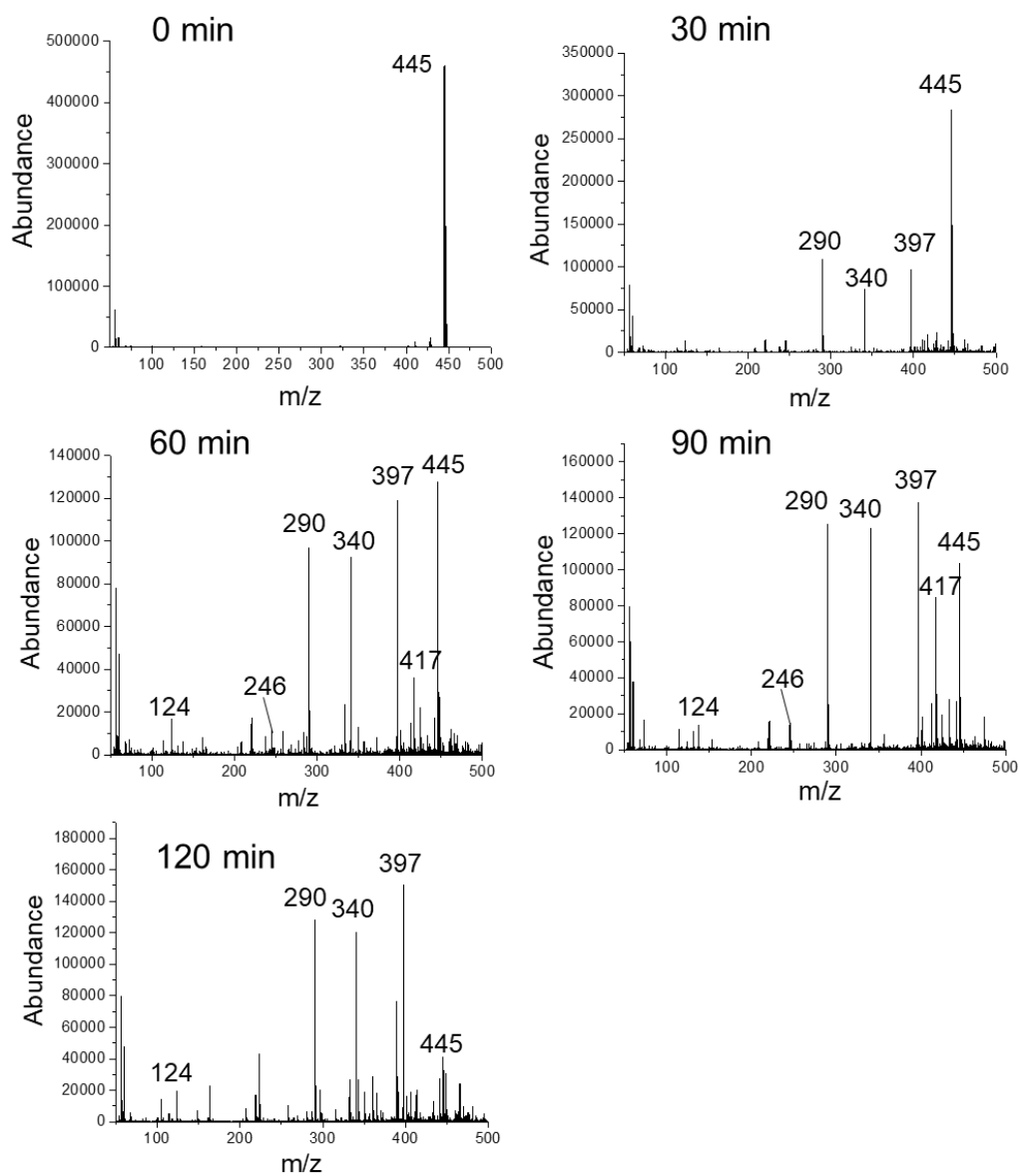


**Fig. S22.** MS values of TC-HCl degradation products at different reaction times as marked over CN4L.

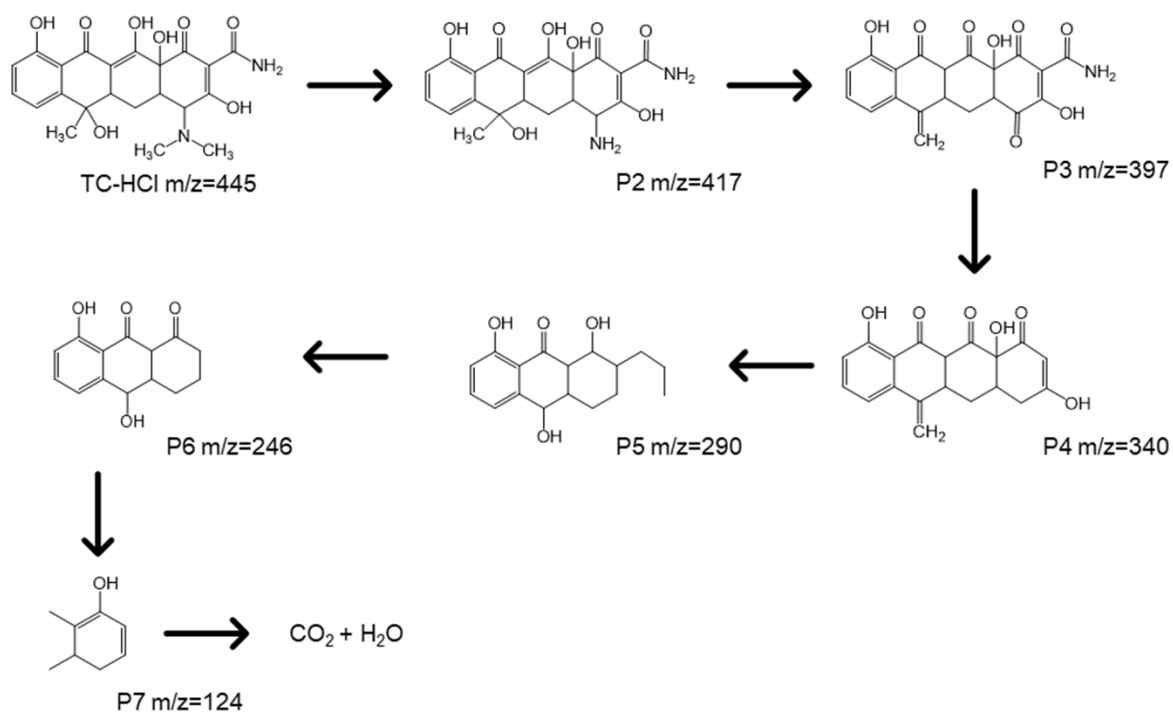


**Fig. S23.** Possible photodegradation pathway of TC-HCl over CN4L.

## References

1. T. Banerjee, F. Podjaski, J. Kröger, B. P. Biswal and B. V. Lotsch, *Nat. Rev. Mater.*, 2021, **6**, 168-190.
2. P. Niu, L.-C. Yin, Y.-Q. Yang, G. Liu and H.-M. Cheng, *Adv. Mater.*, 2014, **26**, 8046-8052.
3. V. Wang, G. Tang, Y.-C. Liu, R.-T. Wang, H. Mizuseki, Y. Kawazoe, J. Nara and W. T. Geng, *J. Phys. Chem. Lett.*, 2022, **13**, 11581-11594.
4. H. Inoki, G. Seo and K. Kanai, *Appl. Surf. Sci.*, 2020, **534**, 147569.
5. J. M. Crowley, J. Tahir-Kheli and W. A. Goddard, III, *J. Phys. Chem. Lett.*, 2016, **7**, 1198-1203.
6. S. T. A. G. Melissen, T. Le Bahers, P. Sautet and S. N. Steinmann, *Phys. Chem. Chem. Phys.*, 2021, **23**, 2853-2859.
7. Y. Zhu, C. Lv, Z. Yin, J. Ren, X. Yang, C.-L. Dong, H. Liu, R. Cai, Y.-C. Huang, W. Theis, S. Shen and D. Yang, *Angew. Chem. Int. Ed.*, 2020, **59**, 868-873.
8. R. Lin, J. Wan, Y. Xiong, K. Wu, W.-c. Cheong, G. Zhou, D. Wang, Q. Peng, C. Chen and Y. Li, *J. Am. Chem. Soc.*, 2018, **140**, 9078-9082.
9. M. Ismael, *J. Environ. Chem. Eng.*, 2020, **8**, 103676.
10. P. B. de Sousa, A. F. Gouveia, J. C. Sczancoski, I. C. Nogueira, E. Longo, M. A. San-Miguel and L. S. Cavalcante, *J. Alloys Compd.*, 2021, **855**, 157377.
11. J. Meng, X. Wang, Y. Liu, M. Ren, X. Zhang, X. Ding, Y. Guo and Y. Yang, *Chem. Eng. J.*, 2021, **403**, 126354.
12. J. Bao, W. Quan, Y. Ning, H. Wang, Q. Wei, L. Huang, W. Zhang, Y. Ma, X. Hu and H. Tian, *Inorg. Chem.*, 2023, **62**, 1086-1094.
13. H. Sun, F. Guo, J. Pan, W. Huang, K. Wang and W. Shi, *Chem. Eng. J.*, 2021, **406**, 126844.
14. X. Zhan, Y. Zhao, Y. Sun, C. Lei, H. Wang and H. Shi, *Chemosphere*, 2022, **307**, 136087.
15. Y. Lin, L. Wang, Y. Yu, X. Zhang, Y. Yang, W. Guo, R. Zhang, Y. Zhai and Y. Liu, *New J. Chem.*, 2021, **45**, 18598-18608.
16. F. Guo, M. Li, H. Ren, X. Huang, K. Shu, W. Shi and C. Lu, *Sep. Purif. Technol.*, 2019, **228**, 115770.
17. Y. Xu, Y. Liang, Z. Yuai, H. Long, Q. He, K. Guo, Y. Zhang, D. Chen, X. Xu and H. Hu, *Ceram. Int.*, 2022, **48**, 24677-24686.